

Fluid Flow Characteristics and Porosity Behavior in Full Penetration Laser Welding of a Titanium Alloy

BAOHUA CHANG, CHRIS ALLEN, JON BLACKBURN, PAUL HILTON,
and DONG DU

In this paper, a computational fluid mechanics model is developed for full penetration laser welding of titanium alloy Ti6Al4V. This has been used to analyze possible porosity formation mechanisms, based on predictions of keyhole behavior and fluid flow characteristics in the weld pool. Numerical results show that when laser welding 3 mm thickness titanium alloy sheets with given laser beam focusing optics, keyhole depth oscillates before a full penetration keyhole is formed, but thereafter keyhole collapses are not predicted numerically. For lower power, lower speed welding, the fluid flow behind the keyhole is turbulent and unstable, and vortices are formed. Molten metal is predicted to flow away from the center plane of the weld pool, and leave a gap or void within the weld pool behind the keyhole. For higher power, higher speed welding, fluid flow is less turbulent, and such vortices are not formed. Corresponding experimental results show that porosity was absent in the melt runs made at higher power and higher welding speed. In contrast, large pores were present in melt runs made at lower power and lower welding speed. Based on the combination of experimental results and numerical predictions, it is proposed that porosity formation when keyhole laser welding may result from turbulent fluid flow behind the keyhole, with the larger the value of associated Reynolds number, the higher the possibility of porosity formation. For such fluid flow controlled porosities, measures to decrease Reynolds number of the fluid flow close to the keyhole could prove effective in reducing or avoiding porosity.

DOI: 10.1007/s11663-014-0242-5

© The Minerals, Metals & Materials Society and ASM International 2014

I. INTRODUCTION

LASER beam welding as a near net-shape fabrication process has attracted attention in automotive, aeronautical, and aerospace industries, because of its high productivity, high automation level, and high utilization rate of materials. In these applications, the use of light metals, such as titanium and aluminum alloys, is particularly beneficial, because of their inherently high strength to weight ratios and great potential for weight saving, which in turn can save energy and decrease associated emissions.

Although laser welding has been proven to be a robust process for producing satisfactory welds in steels, it can be less straightforward to achieve an acceptable weld quality when laser welding titanium and aluminum alloys. One particular concern is the formation of subsurface porosity in the weld metal when laser welding. Achieving consistently acceptably low levels of porosity is currently an

obstacle that prevents wider acceptance of laser welding. Therefore, it is critical to study the formation mechanism(s) contributing to porosity, and hence make progress towards the development of porosity reduction measures. To date, an extensive amount of experimental work and a lesser extent of numerical modeling have been carried out in this area.

Numerical modeling of laser welding can be traced back to the 1970s. However, early models mainly addressed temperature fields, to predict penetration depths developed during laser welding, but did not take the dynamic behavior of fluid flow in the weld pool or the keyhole itself into account.^[1-20] Although helpful in understanding some aspects of laser welding, these early models were not sufficiently sophisticated to assist in analyzing porosity formation mechanisms.

Ki *et al.*^[21,22] presented for the first time a three-dimensional laser welding model in 2002, featuring the self-consistent evolution of a keyhole, together with a full simulation of fluid flow and heat transfer. Using their model, the authors studied how and why simple conduction-mode welding could transform to complex keyhole-mode welding. Their predictions were, however, for mild steels and porosity was not discussed.

Tsai and Zhou *et al.*^[23-26] carried out a series of numerical modeling activities of laser welding processes. They developed mathematical models and associated numerical techniques to handle a number of complicated phenomena present in laser welding, including melt flow and heat transfer, keyhole formation and

BAOHUA CHANG, Associate Professor, is with the State Key Laboratory of Tribology, Department of Mechanical Engineering, Tsinghua University, Beijing 100084, P.R. China, and also with the TWI Ltd, Granta Park, Great Abington, Cambridge CB21 6AL, U.K. Contact e-mail: bhchang@tsinghua.edu.cn CHRIS ALLEN, Principal Project Leader, JON BLACKBURN, Section Manager, and PAUL HILTON, Technology Fellow, are with the TWI Ltd. DONG DU, Professor, is with the State Key Laboratory of Tribology, Department of Mechanical Engineering, Tsinghua University.

Manuscript submitted March 13, 2014.

Article published online November 21, 2014.

collapse processes, *etc.* Using the numerical models they developed, they studied the formation of porosity, and possible porosity control strategies when laser welding aluminum alloys. However, only partial penetration welds were modeled in their work.

Pang *et al.*^[27] used a three-dimensional sharp interface model to investigate a self-consistent keyhole and its associated melt pool dynamics when deep-penetration laser welding. A collapsing free keyhole was predicted under certain low heat input, deep-penetration laser welding conditions. Periodic keyhole collapse and bubble formation were also simulated. Nevertheless, full penetration keyholes were not modeled in this work either.

Zhao *et al.*^[28] simulated molten pool and keyhole phenomena in the laser welding of stainless steel. They found that keyhole depth fluctuated, and that bubbles formed from keyhole collapse and shrinkage, leading to keyhole-induced porosity. Zhang *et al.*^[29] also studied porosity in laser spot welding of a 304 stainless steel numerically. They showed that the keyhole collapsed and liquid metal tended to backfill the keyhole when the laser power was turned off. The formation of pores was closely related to the solidification rate and the back-filling speed. If the back-filling speed of the molten metal was lower than its solidification rate, a pore would form in the final weld.

Although most of this work took the keyhole collapse as the main factor contributing to porosity formation, the work of Amara *et al.*^[30] and Zhang *et al.*^[31] proved that the fluid flow of molten metal in the weld pool could also have a strong influence on porosity formation. Amara *et al.*^[30] showed in their numerical model for partial penetration laser welding of iron that a more uniform fluid flow in the weld pool, and hence fewer pores, could be obtained when a high-speed jet of inert gas was projected onto the melt pool, using a tube inclined at 45 deg pointing backwards onto the pool. Similarly, Zhang *et al.*,^[31] in their numerical modeling of the transient behavior of a molten pool and a keyhole during full penetration laser welding of a titanium alloy, also found that appropriate control of a side gas flow jet acting on molten pool could improve the stability of the molten pool and hence reduce porosity content. This work, however, did not model the dynamic development of keyhole.

An X-ray imaging system together with a high-speed camera has also been used experimentally to visualize the weld pool and keyhole in laser welding, and to analyze their influences on porosity formation.^[32–43] With such a system, Matsunawa *et al.*^[36–39] studied the laser welding of AA5083 aluminum alloy shielded with helium. It was observed that the depth and shape of the keyhole fluctuated violently, with large bubbles being formed intermittently at the bottom of keyhole. If these bubbles became trapped by the solidifying weld pool as they floated up, they remained as porosity. The keyhole was found to be more stable under nitrogen shielding than under helium shielding, and porosity was hardly formed. This was attributed to the formation of AlN on the weld pool surface, by which the motions of the pool surface were greatly suppressed, and the fluctuation of

keyhole was stabilized correspondingly. It was also indicated that the keyhole became more unstable in deeper penetration welding, and larger pores were more likely to appear due to keyhole fluctuations. Square wave power modulation at the eigenfrequency of the molten pool was shown to be effective in decreasing the formation of porosity, due to the stabilization of keyhole perturbations.^[44–46]

Based on experimental observations, Kaplan *et al.*^[47] presented a model to explain pore formation during keyhole collapse after the end of a laser pulse. It was indicated that re-condensation of the metal vapor after pulse termination sucked the surrounding Ar-shielding gas into the keyhole, which then entered the weld zone as bubbles as the keyhole collapsed. These gas bubbles, as a result of the complex molten metal flows in weld pool, were not able to escape prior to solidification and become entrapped as porosity. Blackburn^[48] reconfirmed this mechanism in his studies of the porosity, when keyhole laser welding titanium alloys. It was stated that the porosities were formed as a result of keyhole instability and closure when the laser was turned off, which lead to the presence of shielding gases in the melt pool.

Overall, work carried out to date has made some progress towards understanding the physical processes taking place during laser welding. However, most has concerned partially penetrating welds in materials such as steels or Al alloys, as opposed to fully penetrating welds in a wider range of materials. More complicated interactions between surface tension, recoil force, and gravity are present when the keyhole transfers from a partially to fully penetrating geometry. To date, therefore, keyhole behavior and fluid flow characteristics, in addition to their relationships with porosity formation, when full penetration laser welding, still remain unclear, and numerical models capable of studying the formation mechanisms of porosity in fully penetrated welds remain to be developed.

In this paper, a numerical model has been developed for full penetration laser welding of titanium alloy Ti6Al4V, as implemented using the computational fluid dynamic (CFD) software FLUENT, and validated experimentally. This model has then been used to understand the possible effects on keyhole behavior and weld pool fluid flow characteristics when full penetration laser welding using different process parameters. In combination with experimental results, model predictions have been employed to elucidate porosity formation mechanisms and propose possible reduction measures.

II. NUMERICAL MODELING

A. Simplifications and Assumptions

During laser welding, heat transfer between the laser beam and the workpiece, in addition to mass transfers caused by evaporation, recoil pressure, surface tension, *etc.*, have all been assumed to be influential on weld quality, and have been taken into account in computa-

tional modeling. Laser welding is recognized as a complex problem, from a process modeling perspective, given the presence of multiple phases (solid, liquid, and vapor), the tracking of the free surface of the molten metal weld pool, the dynamic nature of the vapor keyhole, *etc.* Given this, simplifications and assumptions were taken to obtain a computationally efficient approach to the problem. These included

- Fluid flow in the molten metal was assumed to be Newtonian, incompressible, and laminar.
- The three phases (solid, liquid, and vapor) were solved in a single computational domain.
- The Boussinesq approximation was taken, meaning that in buoyancy-driven flow the difference in inertia was neglected, while gravity was considered.
- The existence of the vapor phase (plume) was simplified, with the properties of the weld shielding gas (Ar) being used for that vapor phase.
- The influence of the Knudsen layer on the gas parameters near the keyhole was neglected.

B. Computation Zones and Mesh

A computational fluid dynamics (CFD) model was constructed, using the commercial software ANSYS: Fluent 13.0, for the laser welding of 3 mm thickness titanium alloy Ti6Al4V. The computation zones and dimensions of the CFD model developed are shown in Figure 1. A fixed laser beam was assumed to irradiate the top surface of a workpiece made of titanium alloy (Ti6Al4V), moving with respect to that fixed beam at a speed equal to the welding speed being used. This model consisted of three zones, one representing the workpiece zone and two zones of shielding gas located above and below the workpiece, respectively. This model set-up was chosen as it was applicable to the tracking of the free surface of the keyhole as it evolved using a volume of fraction (VOF) multiphase fluid model, used to determine the shape and dimensions of that keyhole at any given moment in time during the running of a simulation. To save computational time, geometrical symmetry of the workpiece about the welding direction was assumed; thus, only half of the workpiece was included in computation. A three-dimensional mesh was constructed, as shown in Figure 2. This had 257,040 cells, for a 3 mm thickness workpiece. The minimum element size used was $0.025 \times 0.025 \times 0.1 \text{ mm}^3$.

C. Governing Equations

The governing equations for heat and mass transfers during the laser welding process were:

The continuity equation

$$\frac{\partial \rho}{\partial t} + \frac{\partial(\rho u)}{\partial x} + \frac{\partial(\rho v)}{\partial y} + \frac{\partial(\rho w)}{\partial z} + S_m = 0. \quad [1]$$

The momentum equation, in the x axis

$$\begin{aligned} \frac{\partial(\rho u)}{\partial t} + \frac{\partial(\rho uu)}{\partial x} + \frac{\partial(\rho vu)}{\partial y} + \frac{\partial(\rho wu)}{\partial z} &= \frac{\partial}{\partial x} \left(\mu \frac{\partial u}{\partial x} \right) \\ &+ \frac{\partial}{\partial y} \left(\mu \frac{\partial u}{\partial y} \right) + \frac{\partial}{\partial z} \left(\mu \frac{\partial u}{\partial z} \right) - \frac{\partial P}{\partial x} + S_x. \end{aligned} \quad [2]$$

The momentum equation, in the y axis

$$\begin{aligned} \frac{\partial(\rho v)}{\partial t} + \frac{\partial(\rho uv)}{\partial x} + \frac{\partial(\rho vv)}{\partial y} + \frac{\partial(\rho wv)}{\partial z} &= \frac{\partial}{\partial x} \left(\mu \frac{\partial v}{\partial x} \right) \\ &+ \frac{\partial}{\partial y} \left(\mu \frac{\partial v}{\partial y} \right) + \frac{\partial}{\partial z} \left(\mu \frac{\partial v}{\partial z} \right) - \frac{\partial P}{\partial y} + S_y. \end{aligned} \quad [3]$$

The momentum equation, in the z axis

$$\begin{aligned} \frac{\partial(\rho w)}{\partial t} + \frac{\partial(\rho uw)}{\partial x} + \frac{\partial(\rho vw)}{\partial y} + \frac{\partial(\rho ww)}{\partial z} &= \frac{\partial}{\partial x} \left(\mu \frac{\partial w}{\partial x} \right) \\ &+ \frac{\partial}{\partial y} \left(\mu \frac{\partial w}{\partial y} \right) + \frac{\partial}{\partial z} \left(\mu \frac{\partial w}{\partial z} \right) - \frac{\partial P}{\partial z} + S_z. \end{aligned} \quad [4]$$

The energy equation

$$\begin{aligned} \frac{\partial(\rho H)}{\partial t} + \frac{\partial(\rho uH)}{\partial x} + \frac{\partial(\rho vH)}{\partial y} + \frac{\partial(\rho wH)}{\partial z} &= \frac{\partial}{\partial x} \left(k \frac{\partial T}{\partial x} \right) \\ &+ \frac{\partial}{\partial y} \left(k \frac{\partial T}{\partial y} \right) + \frac{\partial}{\partial z} \left(k \frac{\partial T}{\partial z} \right) + S_H, \end{aligned} \quad [5]$$

where u , v , and w denoted the different components of velocity in Cartesian coordinates; ρ , P , H , k , and μ denoted the density, pressure, enthalpy, thermal conductivity, and viscosity, respectively; and S_m , S_x , S_y , S_z , and S_H denoted the source terms of the continuity equation, momentum equations, and energy equation.

D. Boundary Conditions

1. Symmetry plane

On the symmetry plane in the model

$$k \frac{\partial T}{\partial \vec{n}} = 0, \quad [6]$$

$$k \frac{\partial \rho}{\partial \vec{n}} = 0, \quad [7]$$

where \vec{n} was the normal vector of the plane.

2. Side of the computational region

The side of the workpiece (*i.e.*, that plane parallel and opposite to the symmetry plane) was treated as zero-shear wall boundary, with the energy transfer on this surface including convection and radiation, satisfying the following equation:

$$k \frac{\partial T}{\partial \vec{n}} = q_{\text{convection}} + q_{\text{radiation}}. \quad [8]$$

With the convective heat expressed as:

$$q_{\text{convection}} = h_c(T - T_a), \quad [9]$$

and the radiative heat expressed as:

$$q_{\text{radiation}} = \sigma \varepsilon (T^4 - T_a^4), \quad [10]$$

where T was the temperature of the workpiece, T_a was the ambient temperature, h_c was the convection coefficient with shielding gas, σ was the Stefan–Boltzmann constant, and ε was the surface emissivity.

3. Top and bottom surfaces of the computational region

The top and bottom surfaces of the computational region were also treated as zero-shear wall boundaries. The heat transfer at these surfaces obeyed the following equation:

$$k \frac{\partial T}{\partial n} = q_{\text{radiation}} + q_{\text{convection}}. \quad [11]$$

4. End surfaces of the workpiece

The right end surface of the workpiece (as oriented in Figures 1 and 2) was assumed to be a velocity inlet boundary, with the velocity (u_{in}) equal to the welding speed (v_w) and normal to that surface

$$u_{\text{in}} = v_w. \quad [12]$$

The left end surface of the workpiece was assumed to be a pressure outlet boundary.

5. End surfaces of the shielding gas regions

Both the right and left end surfaces of the shielding gas regions were set as pressure outlet boundaries.

E. Free Surface Tracing

To study keyhole formation and dynamics, the evolution of the free surface of the weld pool was

traced using a volume-of-fluid (VOF) method. The VOF function $F(x, y, z, t)$ was defined to track the free surface. The function F took the value of one for a cell full of liquid and zero for a cell full of vapor. A value of F between zero and one indicated a cell at the liquid/vapor boundary. The function F could be expressed as

$$\frac{\partial F}{\partial t} + v \cdot \nabla F = 0, \quad [13]$$

in which v was kinematic fluid viscosity. As noted previously, when considering the gas present in the keyhole, the material properties of the shielding gas, argon, were used.

F. Source Terms

1. Heat source model

The heat input from the laser beam was simplified to a body heat flux. The heat source model used was an adaptive rotated Gaussian heat source. From this model, the energy distribution at a given depth was a Gaussian distribution. However, the energy distribution also changed with the keyhole depth, $d(t)$, in turn a function of time as determined by the VOF method used. The distribution of the heat input was described by the following equation:

$$Q(x, y, z) = \frac{3\eta P}{\pi abd} \exp\left(-\frac{3x^2}{a^2}\right) \exp\left(-\frac{3y^2}{b^2}\right) \exp\left(-\frac{3z^2}{d^2}\right), \quad [14]$$

where P was the input power of laser beam, η the absorption coefficient of laser beam energy, a and b parameters related to the distribution of the energy of the heat source, both set equal to the focal radius of the laser beam, and d was the depth of the heat source, set equal to the depth of keyhole. The depth of keyhole was, in turn, determined during modeling by tracing the bottom of the interface between the molten pool and shielding gas.

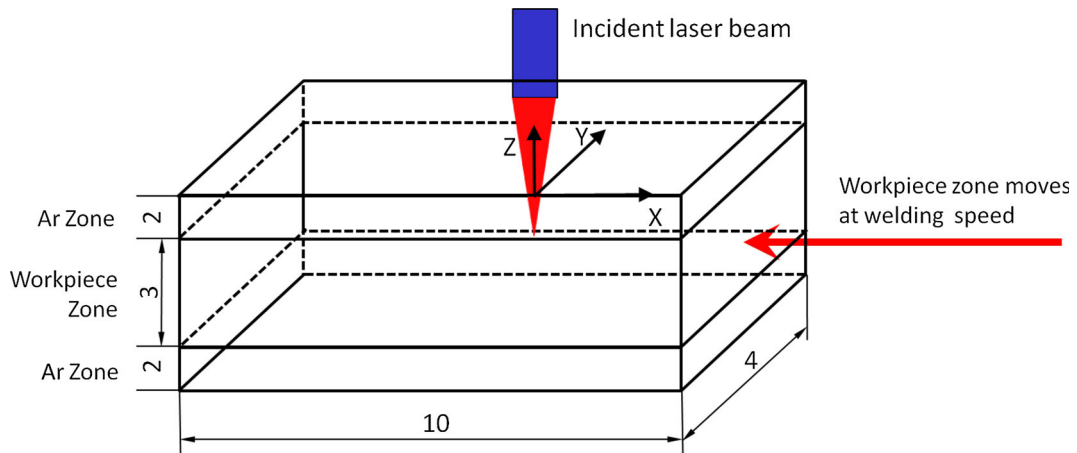


Fig. 1—Dimensions of the section modeled (in mm).

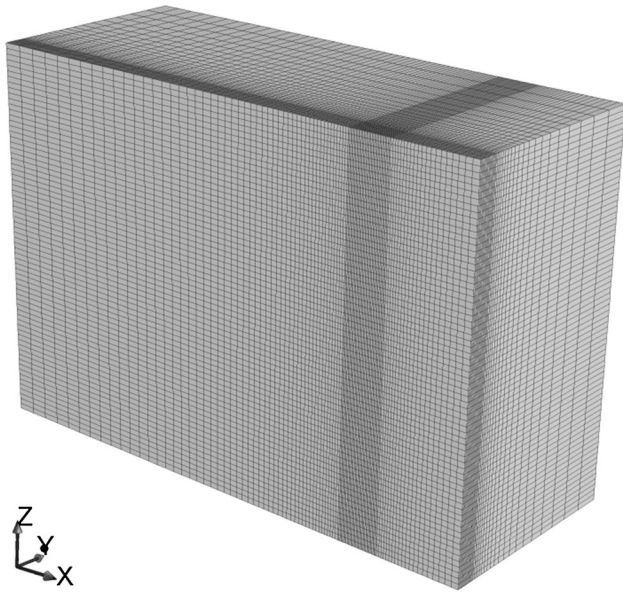


Fig. 2—The mesh constructed for CFD modeling.

2. Melting/solidifying latent

The enthalpy-porosity method was used to handle melting and solidification phase changes, with which the corresponding momentum and energy equations can be solved using a fixed mesh, without the need to track the liquid/solid interface and to specify a boundary at its location. In the enthalpy-porosity method, the fraction of liquid, f_l , was defined as:

$$f_l = \begin{cases} 0, & T < T_s \\ 1, & T > T_s \\ \frac{T-T_s}{T_1-T_s}, & T_s < T < T_1 \end{cases}, \quad [15]$$

in which, T_s and T_1 corresponded to the solidus and liquid temperatures of the workpiece, respectively. Accordingly, the dependency of the change in enthalpy (ΔH_m) with temperature, resulting from a solid/liquid phase change, could be described as

$$\Delta H_m = \begin{cases} L, & T > T_1 \\ f_l L, & T_s < T < T_1 \\ 0, & T < T_s \end{cases}, \quad [16]$$

in which L was the latent heat associated with the melting/solidifying phase change. This change in enthalpy due to the melting/solidifying latent heat was taken into account in the numerical model by adding the following source term to the energy equation:

$$S_h = -\left(\frac{\partial}{\partial t}(\rho\Delta H_m) + \frac{\partial}{\partial x}(\rho u\Delta H_m) + \frac{\partial}{\partial y}(\rho v\Delta H_m) + \frac{\partial}{\partial z}(\rho w\Delta H_m)\right) + \frac{\partial}{\partial x}(\rho u_x\Delta H_m). \quad [17]$$

3. Pressure on the keyhole

The forces acting on the molten surface around the keyhole included recoil pressure P_r , surface tension P_σ , radiation pressure P_1 , hydrostatic pressure P_g , and hydrodynamic pressures P_v . Consequently, the pressure on the keyhole surface satisfied the following equation:

$$P = P_r + P_1 + P_\sigma + P_g + P_v. \quad [18]$$

P_r and P_1 were driving forces to form (open) a keyhole, while P_σ and P_g prevented the formation of a keyhole. Compared with the other pressures, P_1 was very small and therefore assumed negligible. Instead, recoil pressure, surface tension, and hydraulic pressures were considered in this work. Recoil pressure is a complicated phenomenon to describe, but a widely applied expression is Reference 17:

$$P_r = 0.54P_0 \exp\left(\frac{\Delta H_v}{RTT_v} \frac{T - T_v}{T_v}\right), \quad [19]$$

where P_0 was the atmospheric pressure, ΔH_v the latent heat of evaporation of the liquid, T_v the liquid-vapor equilibrium temperature, T the temperature at the keyhole surface, and R the universal gas constant.

Surface tension P_σ was a function of temperature, and obeyed the following equation:

$$P_\sigma(T) = 1.557 - 1.5 \times 10^{-4} \times (T - T_m), \quad [20]$$

where T was the temperature at the keyhole surface and T_m the melting point of the workpiece.

Hydraulic pressures, P_h , which included both hydrostatic and hydrodynamic pressures, could be calculated as follows:

$$P_h = P_g + P_v = gh + \frac{v^2}{2g}, \quad [21]$$

where h and v were the height and velocity of the fluid in the weld pool, respectively.

4. Buoyancy force

The density of the metal in the weld pool varied with temperature. In the model, the buoyancy force due to the density gradient was expressed as

$$S_B = \rho g \beta (T - T_m), \quad [22]$$

where β was the thermal expansion coefficient, T the temperature of molten metal, and T_m the melting point of the workpiece.

G. Numerical Method

The governing equations presented in Section II-C, the boundary conditions presented in Section II-D, and source terms presented in Section II-F were handled as follows:

- The governing Eqs. [1] through [5] were solved iteratively, to obtain the velocity, temperature, and pressure distributions for the fluid domain.
- Equation [13] was solved to calculate the free surface of the keyhole.

- (c) The pressures and the surface tension on the keyhole surface, and the buoyancy force in the molten pool, were treated as the source terms in the momentum Eqs. [2] through [4].
- (d) The heat source and the heat transfer boundary conditions on the keyhole surface were treated as the source terms in the energy Eq. [5].
- (e) The boundary conditions were updated, and steps b-d were repeated, until the final time in the modeling simulation was reached.

User defined functions (UDFs) were written in C languages to implement the model described above, and to realize the source terms of the controlling equations and boundary conditions.

Table I lists the material properties parameters and physical constants used in numerical modeling.

III. EXPERIMENTS

Titanium alloy (Ti6Al4V) sheets of 3 mm in thickness were used in experimental trials. Laser welding was carried out using an IPG Photonics YLS-5000 Yb-fiber laser, with an output wavelength of 1070 ± 10 nm. A $150 \mu\text{m}$ core diameter optical fiber was used to deliver the beam from the laser source to the processing head.

A Vision Research Phantom 7 high-speed camera was used to observe the keyhole and weld pool behavior. A Cavitar HF diode laser ($\lambda = 808$ nm) was used to illuminate the weld zone. A resolution and frame rate of 512×256 pixels and 10,000 frames per second were used, respectively. The videos recorded were analyzed to assist in the validation of the CFD model being developed, as well as to study the dynamic behavior of keyhole and weld pool experimentally. This set-up is illustrated in Figure 3.

Based on previous experience at TWI, melt run trials were carried out using two different combinations of laser beam power and traverse speed, as listed in

Table II, to evaluate the effect of process parameters on the resulting porosity content of the melt runs made. Argon, of purity 99.99 pct, was used as the shielding gas to protect the melt bead from oxidation.

The porosity contents of all melt runs were evaluated by radiographic examination, measuring the cumulative length of porosity in each. In addition, cross- and longitudinal-sections were prepared of selected melt runs, to determine the morphologies of the pores in those cases.

IV. RESULTS

A. Validation of the Computational Model

The initial validity of the numerical model developed was examined by comparison of its predictions with the

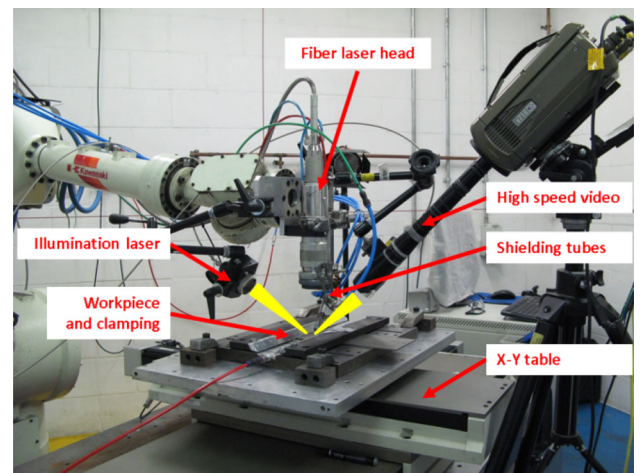


Fig. 3—Equipment set up for laser welding and high-speed video monitoring.

Table I. Material Parameters and Physical Constants

Property	Titanium Alloy Ti6Al4V	Ar
Density, ρ , (kg/m ³)	4420	1.62
Atomic mass, m (kg/kgmol)	44.2	39.9
Specific heat, C_p [J/(kg K)]	546	520.6
Thermal conductivity, λ [W/(m K)]	34.6	0.0158
Viscosity, μ [kg/(m s)]	3.25×10^{-3}	2.125×10^{-5}
Thermal expansion coefficient, β (1/K)	11.0×10^{-6}	—
Melting temperature, T_m (K)	1923 K (1650 °C)	—
Evaporation temperature, T_v (K)	2740 K (2467 °C)	—
Melting enthalpy, ΔH_m (J/kg)	2.86×10^5	—
Evaporation enthalpy, ΔH_v (J/kg)	2.84×10^7	—
Surface tension coefficient, P_σ (N/m)	See Eq. [20]	—
Atmospheric pressure, p_0 (Pa)		101,300
Ideal gas constant, R [J/(K mol)]		8.31
Boltzmann's constant, σ (J/K)		1.38×10^{-23}
Convection coefficient, h_c [W/(m ² K)]		10
Gravity acceleration, g (m/s ²)		9.81
Surface emissivity, ε		0.14

Table II. Process Parameters Used in Melt Run Trials

No. of Sample	Power (kW)	Welding Speed (m/min)	Materials Thickness (mm)	Focal Position (mm)
Case 1	1.5	1.0	3	0
Case 2	3.0	2.5	3	0

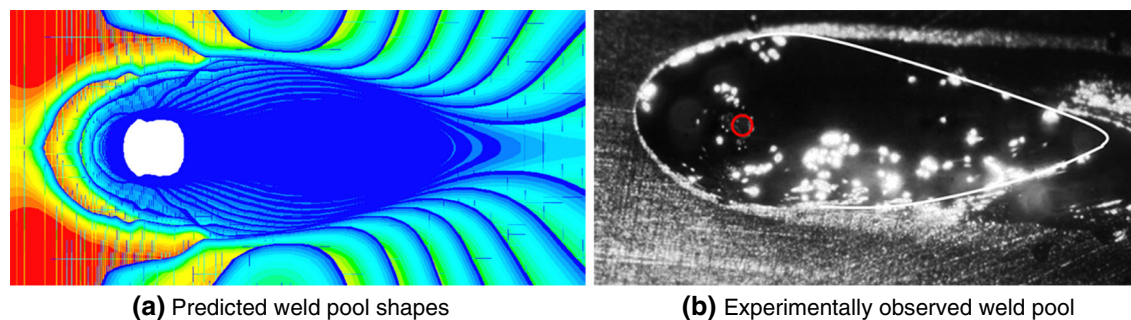


Fig. 4—Plan views of predicted weld pool shape (a), vs experimentally observed weld pool (b), when welding using a laser beam power of 1.5 kW at a speed of 1.0 m/min.

results of high-speed video imaging. In particular, the shapes and dimensions of the weld pools observed during welding were compared with those predicted by the model.

Using a laser power of 1.5 kW, a welding speed of 1.5 m/min, and a beam radius of 0.23 mm, the predicted shape of the weld pool is shown in Figure 4(a). The dark blue region shown represents a plan view of the interface of vapor/liquid (with a volume fraction of workpiece of ~ 0.9 , from CFD modeling), showing the shape of the weld pool present, whose upper surface is depressed below that of the surrounding solid workpiece. A comparison with Figure 4(b) shows, the predicted weld pool compared well with that observed using high-speed video.

V. NUMERICAL MODELING RESULTS

A. Keyhole Developments During Welding

1. Variations of keyhole depth

Simulated keyhole depths over time (during model simulations) are shown in Figure 5. Figure 5(a) shows the variations with time in keyhole depth for the two sets of welding conditions listed previously in Table II. In both cases, keyhole depth increased at the beginning of the simulation, until a full penetration state was reached. After that, no further changes in keyhole depth were predicted (*i.e.*, the keyhole remained fully penetrating at all times, for both conditions). When the laser power was turned off at the end of the simulations, the keyhole depth decreased quickly, in both cases. The values of keyhole depths at the final stage of the simulation were >0 , in both cases. This reflects the depths of the stop craters predicted to be present after each keyhole has closed completely at the end of each simulation.

Figure 5(b) shows the variations in keyhole depth at the start of the two simulations in more detail. As

shown, keyhole depth did not develop monotonically, instead fluctuating with increasing simulation time until a fully penetrating keyhole was established (this establishment time depending on the welding conditions being simulated). This observation suggested certain instability in the dynamic characteristics of the keyholes, at least at the beginning of welding.

The depth of the higher laser beam power keyhole was predicted to increase slightly faster than that of the lower power keyhole. The former reached a fully penetrating state after 30.3 ms, rather than the latter's 34.9 ms.

Furthermore, abrupt changes in keyhole depth were predicted when the lower power keyhole first achieved full penetration. This could imply that this keyhole was inherently less stable than a higher laser power keyhole.

2. Cross-sections of keyholes at different time

Figure 6 shows the predicted evolution of the keyhole during laser welding, using welding parameters of 1.5 kW laser power, 1.0 m/min welding speed. In this simulation, the laser beam was assumed present for the first 480 ms of the simulation, and was then turned off.

As Figure 6(a) shows, a partial penetration keyhole was formed within 10 ms after the start of the application of beam power. This keyhole was predicted to have a gas pore within it. This suggested that fluid flow was unstable during the early formation of the keyhole.

After 50 ms, the keyhole became fully penetrating, as shown in Figure 6(b). The surfaces of the keyhole walls were not smooth, however, and contained undulations. This also suggested turbulence during at least the initial development of the keyhole.

Aside from this, the keyhole itself appeared stable once fully penetrating ($t > 50$ ms). Keyhole collapses were not predicted, Figures 6(c) through (e). The keyhole was predicted to close within 20 ms after the laser power input was turned off, leaving concave craters at both top and bottom surfaces of the workpiece,

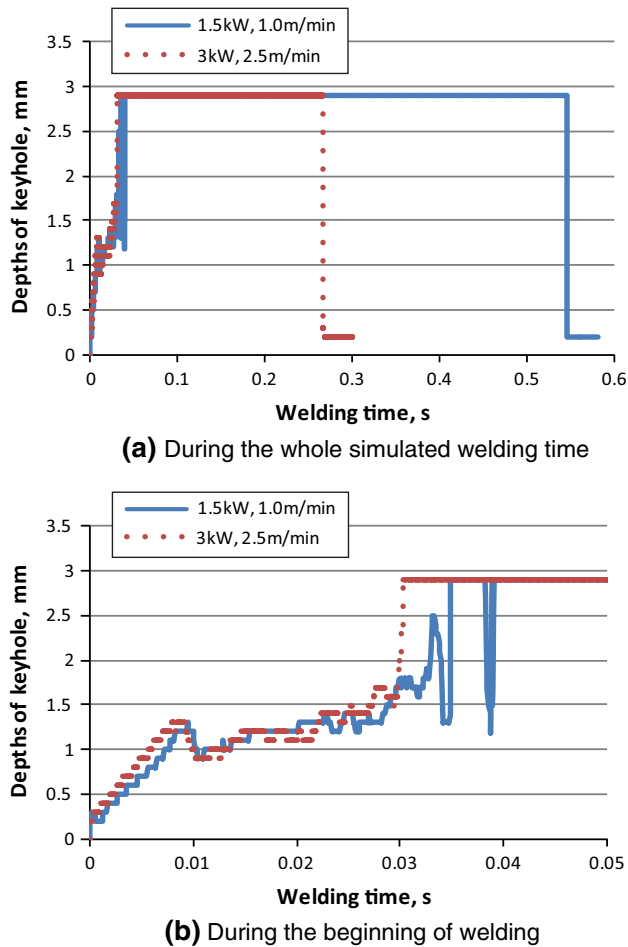


Fig. 5—Variations in the depths of keyholes for two simulated welding conditions.

Figure 6(f). This agreed with the weld pool concavity predicted, an example being shown previously in Figure 4(a).

Figure 7 shows the simulated evolution of the keyhole cross section during laser welding, using welding parameters of laser power of 3.0 kW, and welding speed of 2.5 m/min. In this simulation, the laser beam was assumed present for the first 250 ms of the simulation, and was then turned off.

Akin to the previous case, this simulation suggested that it appeared possible to entrap pores within the melt pool at the beginning of welding, when a narrow, partial penetration keyhole was present, Figure 7(a). In this case, the keyhole was then predicted to expand dynamically, as shown in Figures 7(b) through (e). Keyhole closure was predicted to occur, and slightly concave craters left, within 10 ms after the laser beam power has been switched off, Figure 7(f).

Simulation results for both cases suggested that instabilities existed in partial penetration keyholes present at the beginning of laser irradiation, but that these keyholes appeared stable once full penetration has been reached, with no periodic collapses being predicted. This behavior was predicted to be similar for both sets

of welding conditions simulated. Nevertheless, the diameter of the keyhole was predicted to be smaller and the keyhole wall more undulating when welding with higher laser power at higher speed.

3. Fluid flow characteristics during welding

The fluid flow fields were also computed for these two different sets of welding parameters. Figure 8 shows the fluid flow velocities at the workpiece/vapor interface, *i.e.*, at the surface of the workpiece, for the case of a 1.5 kW beam traversing at 1 m/min, once the welding process has been predicted to reach a steady state. Figure 9 shows the corresponding results for the case of a 3 kW beam at 2.5 m/min.

Both Figures 8(a) and 9(a) show that fluid flow was predicted to be at its fastest in the vicinity of the keyhole. From Figures 8(b) and 9(b), the predicted complexity of fluid flow at the keyhole surface was apparent, occurring in all directions, including vertically upwards, downwards, and laterally.

Aside from at the keyhole surface, the molten metal in the melt pool was predicted to flow backward and downwards around the keyhole as the keyhole advanced. When welding with a 1.5 kW beam at 1 m/min, a vortex was predicted to form behind the keyhole. By contrast, such a vortex was not predicted when welding using a 3.0 kW beam at 2.5 m/min.

4. Development of weld pool during welding

Figure 10 shows the predicted evolution of the weld pool when welding with a 1.5 kW beam at 1.0 m/min. As Figure 10 shows, the weld pool was predicted to grow in both length and width until after ~400 ms has elapsed, by which time a steady state was reached. Notably, a separation of fluid along the symmetry plane was predicted to form in the weld pool behind the keyhole, Figure 10(c). This suggested the formation of cavity in the weld pool behind the keyhole and the possible entrapment of gas at this position, under these welding conditions.

Figure 11 shows the predicted evolution of the weld pool when welding with a 3.0 kW beam at 2.5 m/min. In this case, a steady state was predicted to be reached after ~150 ms, Figure 11(c). A separation of fluid along the symmetry plane of the weld pool behind the keyhole was not observed in this case.

Comparing the model predictions for these two cases, it was seen that the predicted width of the weld pool and the diameter of the keyhole were both significantly larger when laser welding with the lower welding speed, in spite of using the lower laser beam power.

B. Experimental Results

1. Porosity contents in melt runs

The porosity contents of the melt runs were examined using X-ray radiography. The photographs of their top beads and X-ray radiographs of two selected full penetration melt runs, are shown in Figure 12. More details of the porosity contents are listed in Table III.

Porosity was not detected in melt run with higher laser power and welding speed, but was found in melt

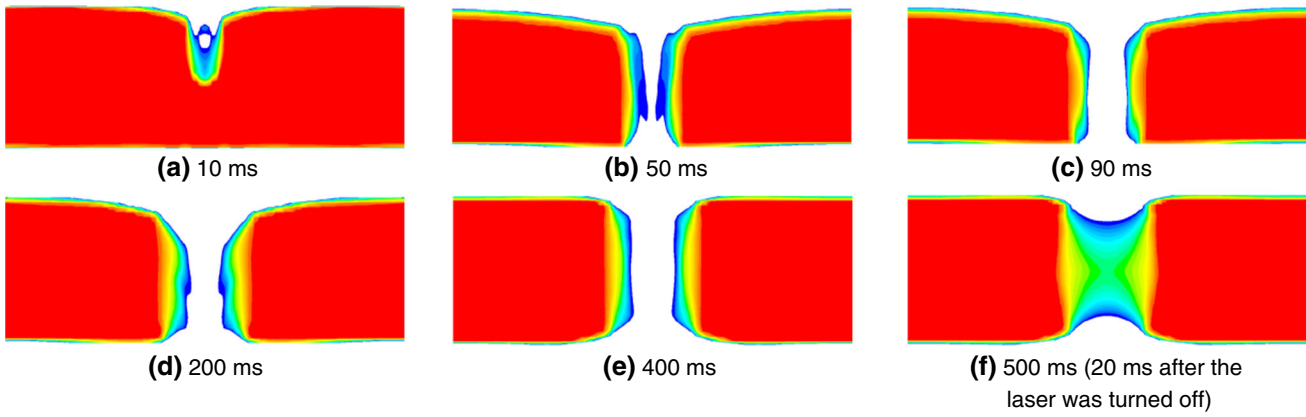


Fig. 6—Predicted cross sections of keyholes at different times for welding conditions of 1.5 kW and 1.0 m/min.

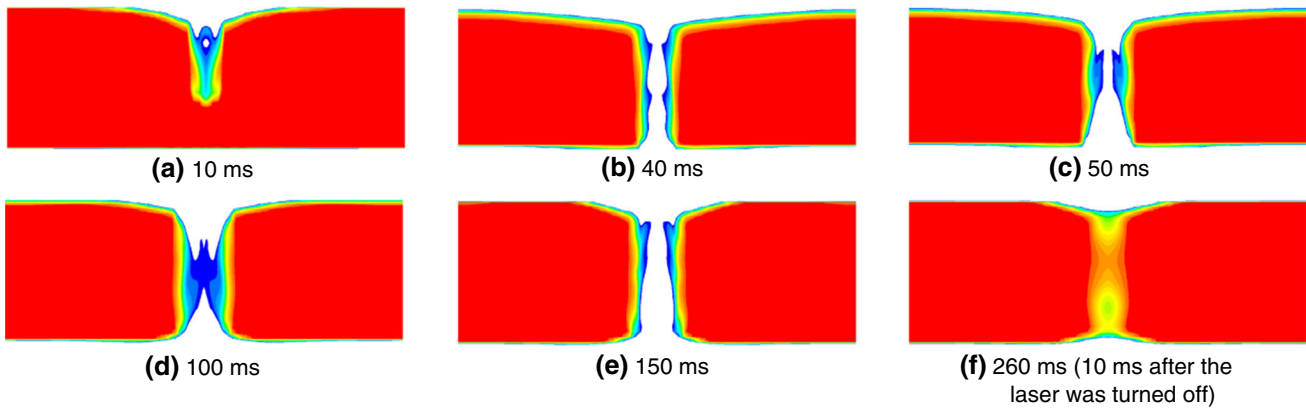


Fig. 7—Predicted cross sections of keyholes at different times for welding conditions of 3.0 kW and 2.5 m/min.

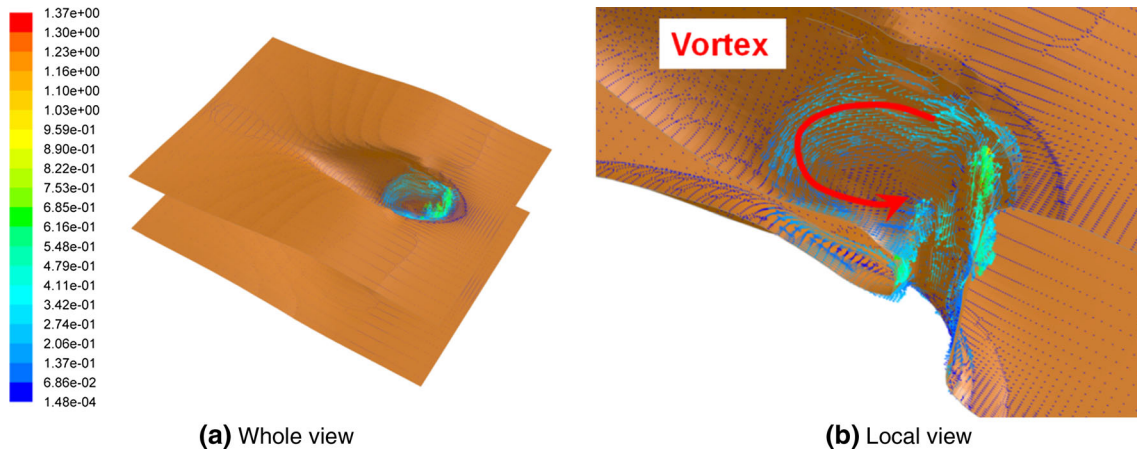


Fig. 8—Fluid flow velocities predicted at the surface of the workpiece when laser welding using a 1.5 kW beam at 1.0 m/min.

run with lower laser power and welding speed. For welding conditions of case 1, large pores (maximum 0.9 mm in diameter) were formed, distributed relatively randomly along the length of the melt run, with accumulative length of 4.9 mm.

2. Pore morphologies in melt runs

Cross sections were prepared of those melt runs containing porosity, from selected locations (where

X-ray radiography detected porosity), to give an indication of the sizes and shapes of the pores present. Cross sections of melt runs apparently free of pores in the main body of the melt run were also prepared, for comparison purposes. The cross sections are shown in Figure 13. The large size and/or irregular shape of pores present in melt run Case 1 can be seen in Figure 13(a).

Longitudinal sections were also made through the stop crater of these two melt runs. These are shown in

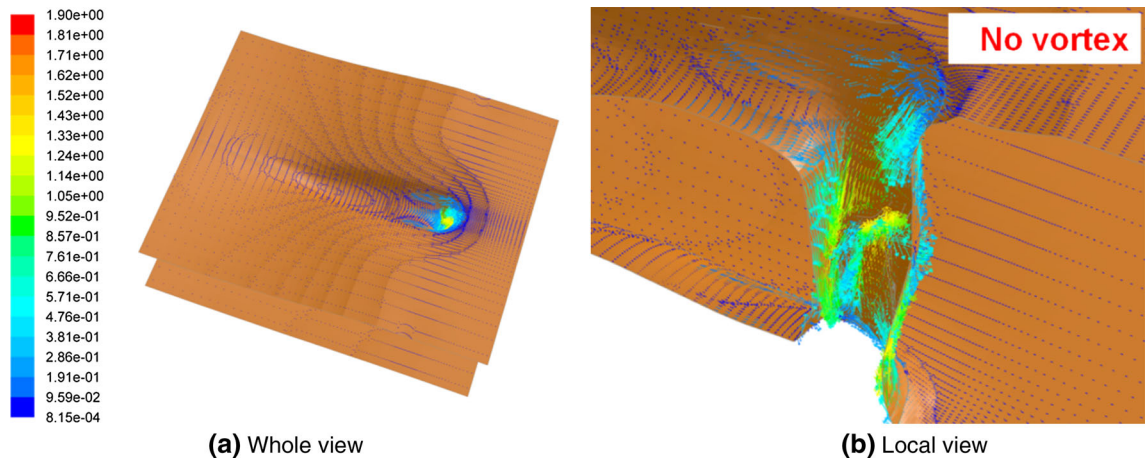


Fig. 9—Fluid flow velocities predicted at the surface of the workpiece when laser welding using a 3.0 kW beam at 2.5 m/min.

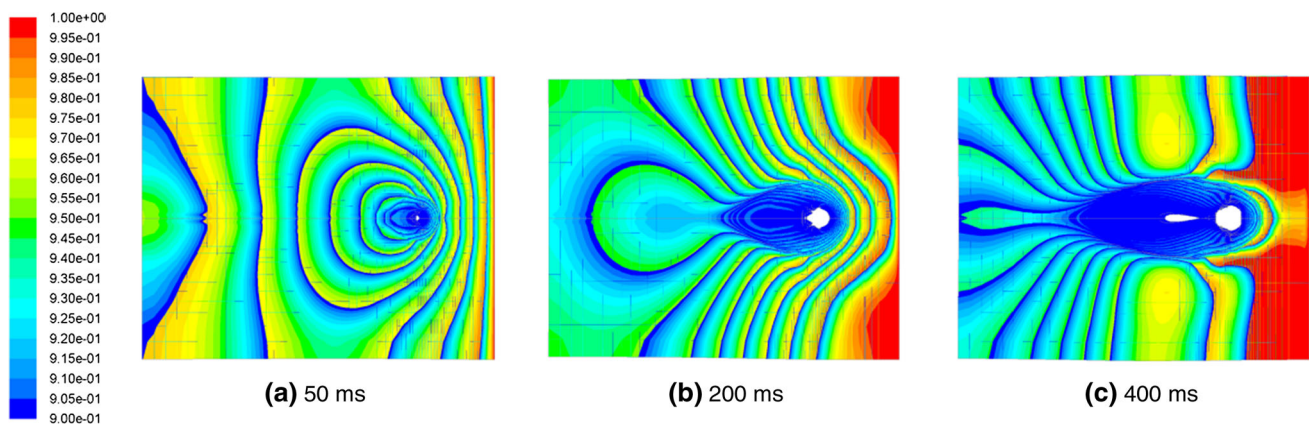


Fig. 10—Shapes and dimensions of the weld pool at different times, for welding conditions of 1.5 kW and 1.0 m/min.

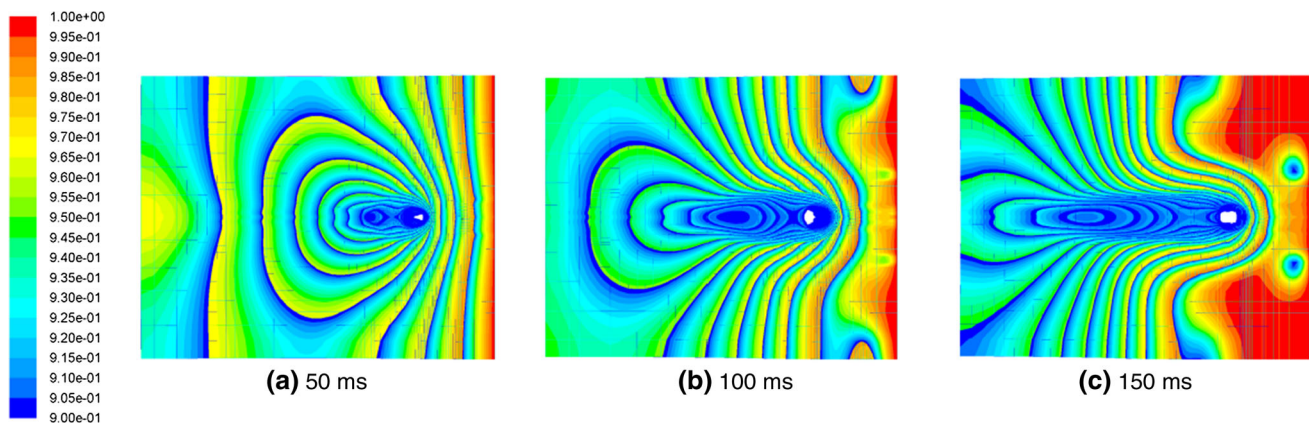


Fig. 11—Shapes and dimensions of the weld pool at different times for welding conditions of 3.0 kW and 2.5 m/min.

Figure 14. As shown, only one large isolated pore was detected in melt run Case 2. Conversely, clusters of pores were present in the stop region of melt run Case 1.

VI. DISCUSSION

To date, many studies have been performed to study the formation of porosity in laser welding. Results show

that the mechanisms behind the formation of porosity in laser welds can be various and complex. In addition to the entrainment of gas-related porosity from sources of contamination, pores can also arise from the instabilities in the keyhole (vapor cavity), with incorrect choice of welding parameters, entrapment of shielding and/or atmospheric gases, and entrapment of metal vapor.

In the current work, numerical modeling and high-speed video analysis of corresponding melt run experiments has sought, but failed, to establish if an unequiv-

ocal relationship exists, during laser welding of 3 mm thickness Ti6Al4V, between keyhole stability (and hence welding parameters) and porosity levels. Keyhole depths were predicted to oscillate before full penetration was achieved, suggestive of keyhole instability during the first moments of laser/material interaction, but thereafter the keyholes, for the different welding conditions modeled in this work, were predicted to remain stable. Consequently, it did not seem that the formation of porosity in the melt runs could be attributed to keyhole collapses.

Nevertheless, differences in porosity content, for identical material preparations and shielding arrangements, yet with changes in welding conditions, were detected experimentally. This in turn suggested that another mechanism was at play, related to which welding conditions were being used.

Numerical modeling predictions suggested that this mechanism might be related to differences in fluid flow patterns in the weld pool behind the keyhole with changes in welding conditions. Modeling predicted that a 'gap' (a cavity owing to separating currents molten metal), as shown previously in Figure 10(c), was formed in the weld pool, with associated vortices, when using lower laser powers and speeds. This could explain the higher porosity content observed when welding with these conditions. By contrast, no 'gap' was predicted to form when using higher laser powers and speeds, correlating with the much lower porosity content observed experimentally. Such differences in fluid flow may also be reflected by experimental results from the stop craters of the corresponding melt runs. A series of large pores was present in the stop region of the melt run made with lower power at lower speed, as shown in Figure 14(a). Conversely, only a single large pore has formed in the stop region of the melt run made using higher power at a higher speed. The former could be the result of eddying flow fluids in the weld pool around the closing keyhole, and the latter the result of a more quiescent keyhole closure once the laser beam has been turned off.

In both cases, the flow of molten metal around the keyhole can be compared with a classical fluid

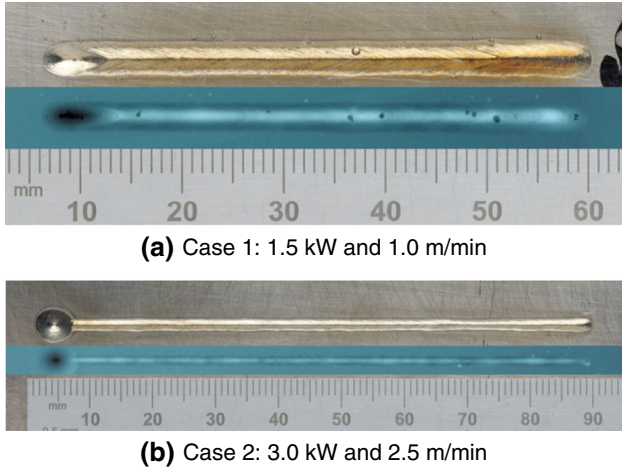


Fig. 12—Top beads (above) and X-ray radiographs (below) of two selected full penetration melt runs.

Table III. Porosity of Full Penetration Melt Runs in 3-mm Thickness Ti6Al4V

Sample Identity	Case 1	Case 2
Thickness (mm)	3	3
Laser power (kW)	1.5	3.0
Welding speed (m/min)	1.0	2.5
Maximum diameter of isolated pore (mm)	0.9	0
Minimum spacing between two pores (mm)	0.4	—
Cumulative length of porosity (mm)	4.9	0
Porosity area ratio (pct)	1.99	0

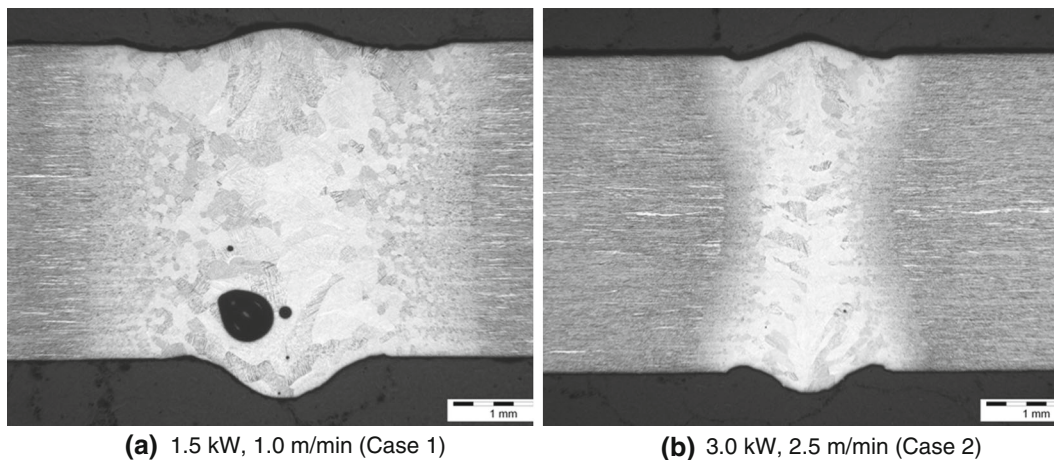


Fig. 13—Cross sections of two melt runs.

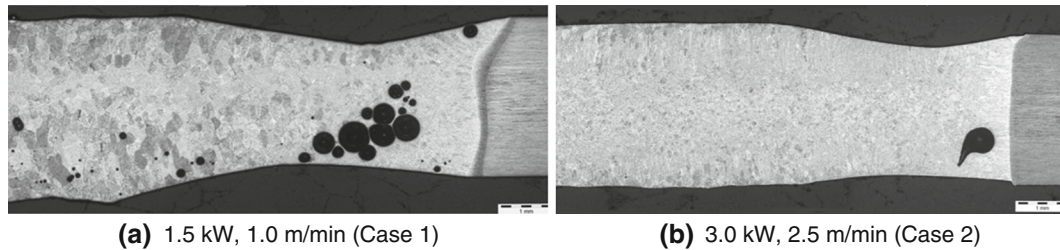


Fig. 14—Longitudinal sections through the stop craters of two melt runs.

mechanics problem that of flow past a circular cylinder. In the case of flow past a cylinder, unstable flow (referred to as von Karman vortex street) forms when the Reynolds number exceeds a value of 60.^[49] The instability of the flow will then continue to increase with increasing Reynolds number. Here, the Reynolds number is defined as

$$\text{Re} = \frac{\rho v L}{\mu}, \quad [22]$$

in which ρ is the density of the fluid, v the mean velocity, μ the dynamic viscosity, and L is a characteristic length.

When welding with a 1.5 kW beam at 1 m/min, and assuming an average velocity of 0.3 m/s in the weld pool predicted from modeling, taking the diameter of the keyhole as the characteristic length, of 0.9 mm (as estimated from numerical results), and assuming a density of 4420 kg/m³, and a viscosity of 0.00325 Pa s, a value of $\text{Re} = 367$ was obtained. This was significantly greater than the critical value of 60. With this value, fluid flow would be predicted to become turbulent, as the molten metal flowed around the keyhole, becoming unstable and forming vortices behind the keyhole. As a result, the molten metal would flow away from the symmetry plane of the weld pool, forming a gap (as predicted numerically), which in turn would lead to a greater tendency to entrap gas, resulting in a higher porosity content after solidification.

In the second case, welding with a 3 kW beam at 2.5 m/min, the average velocity in the weld pool was similar (0.2 to 0.3 m/s) but the keyhole diameter was smaller (~0.4 mm in diameter, from modeling), resulting in a smaller Re value of 163. This could indicate that there would be less turbulence in the fluid flow behind the keyhole, and that the corresponding tendency to entrap gas and form porosity would be reduced.

In such fluid flow controlled situations, methods to decrease the Reynolds number in the vicinity of the keyhole should prove effective in reducing the associated porosity content. Referring to Eq. [22], it can be deduced that for a material with a given density and viscosity, decreasing the flow velocity and/or the diameter of keyhole will decrease the Reynolds number, and could therefore result in lower porosity levels. Such a deduction seems borne out by experiment, using a more focused laser has led to welds with a lower porosity content, as reported previously.^[48] The laser beam with the smaller nominal diameter is anticipated to generate a smaller diameter keyhole, with therefore less turbulent

flow in the molten metal behind it. The resulting porosity content would then be reduced.

VII. CONCLUSIONS

- When laser welding 3-mm thickness Ti6Al4V alloy sheets with the laser and focusing optics used in this work, porosity was absent in a melt run made with higher power (3 kW) and higher welding speed (2.5 m/min), except for only one large, single pore formed in the stop region.
- By contrast, a cumulative length of porosity of 4.9 mm was present in a melt run made with lower power (1.5 kW) at lower speed (1 m/min), along with a series of large pores being present in the stop region.
- Numerical modeling of the experimental work carried out predicted that although keyhole depths can oscillate before full penetration is achieved, for both sets of welding conditions, thereafter keyhole collapses were not predicted to occur.
- For lower power and lower welding speed conditions, the fluid flow behind the keyhole was predicted to be turbulent and unstable, forming vortices. The molten metal was then predicted to flow away from the symmetry plane of the weld pool, and leave a gap or separation within the molten metal behind the keyhole.
- For higher power and welding speed conditions, the fluid flow was predicted to be less turbulent, without vortex formation.
- These numerical predictions, correlated with experimental observations, suggested that in keyhole laser welding, a porosity formation mechanism can exist resulting from the onset of turbulent fluid flow behind the keyhole. This onset appeared associated with the welding conditions being used, and the corresponding Reynolds number for the flow around the keyhole.
- In such fluid flow controlled situations, measures to decrease the Reynolds number of this flow should prove effective in reducing the porosity of laser welds.

ACKNOWLEDGMENTS

This research was supported by a Marie Curie International Incoming Fellowship with the 7th European

Community Framework Programme (Grant Nos. 253487; 919487), whose financial support is gratefully appreciated. Thanks also go to Mathew Spinks and Paul Fenwick of TWI Ltd for performing the welding trials.

REFERENCES

1. D.T. Swift-Hook and A.E.F. Gick: *Weld. J.*, 1973, vol. 52 (11), pp. 492s–99s.
2. J.G. Andrews and D.R. Atthey: *J. Phys. D Appl. Phys.*, 1976, vol. 9, pp. 2181–94.
3. P.G. Klemens: *J. Appl. Phys.*, 1976, vol. 47, pp. 2165–74.
4. H.E. Cline and T.R. Anthony: *J. Appl. Phys.*, 1977, vol. 48 (9), pp. 3895–3900.
5. J. Mazumder and W.M. Steen: *J. Appl. Phys.*, 1980, vol. 51 (2), pp. 941–47.
6. M. Davis, P. Kapadia, and J. Dowden: *Weld. J.*, 1986, vol. 65 (7), pp. 167–72.
7. J. Dowden, N. Postacioglu, M. Davis, and P. Kapadia: *J. Phys. D*, 1987, vol. 20, pp. 36–42.
8. W.M. Steen, J. Dowden, M. Davis, and P. Kapadia: *J. Phys. D*, 1988, vol. 21, pp. 1255–60.
9. N. Postacioglu, P. Kapadia, and J. Dowden: *J. Phys. D*, 1991, vol. 24 (1), pp. 15–20.
10. J. Mazumder, M.M. Chen, C.L. Chan, D. Voelkel, and R. Zehr: *Proc. of Symposium on Joining of Materials for 2000 AD*, 1991, 693–708.
11. K. Mundra, T. DebRoy, T. Zacharia, and S.A. David: *Weld. J.*, 1992, vol. 71 (9), pp. 313s–20s.
12. J. Kroos, U. Gratzke, and G. Simon: *J. Phys. D*, 1993, vol. 26, pp. 474–80.
13. E.A. Metzbower: *Metall. Trans. B*, 1993, vol. 24B, pp. 875–80.
14. W. Sudnik, D. Radaj, and W. Erofeew: *J. Phys. D Appl. Phys.*, 1996, vol. 29, pp. 2811–17.
15. V.V. Semak, B. Damkroger, and S. Kempka: *J. Phys. D*, 1999, vol. 32, pp. 1819–25.
16. H. Zhao and T. DebRoy: *J. Appl. Phys.*, 2003, vol. 93 (12), pp. 10089–96.
17. X. Jin, L. Li, and Y. Zhang: *J. Phys. D*, 2002, vol. 35 (18), pp. 2304–10.
18. X. Jin, P. Berger, and T. Graf: *J. Phys. D*, 2006, vol. 39 (21), pp. 4703–12.
19. J.H. Cho and S.J. Na: *J. Phys. D*, 2006, vol. 39 (24), pp. 5372–78.
20. R. Rai and T. DebRoy: *J. Phys. D*, 2006, vol. 39 (6), pp. 1257–66.
21. H. Ki, P.S. Mohanty, and J. Mazumder: *Metall. Mater. Trans. A*, 2002, vol. 33A, pp. 1817–30.
22. H. Ki, P.S. Mohanty, and J. Mazumder: *Metall. Mater. Trans. A*, 2002, vol. 33A, pp. 1831–42.
23. J. Zhou, H.L. Tsai, and P.C. Wang: *ASME J. Heat Transf.*, 2006, vol. 128 (7), pp. 680–90.
24. J. Zhou and H.L. Tsai: *J. Phys. D*, 2006, vol. 39 (24), pp. 5338–55.
25. J. Zhou and H.L. Tsai: *ASME J. Heat Transf.*, 2007, vol. 129 (8), pp. 1014–24.
26. J. Zhou and H.L. Tsai: *J. Heat Mass Transf.*, 2007, vol. 50 (11–12), pp. 2217–35.
27. S. Pang, L. Chen, J. Zhou, Y. Yin, and T. Chen: *J. Phys. D*, 2011, vol. 44 (2), p. 025301.
28. H.Y. Zhao, W.C. Niu, B. Zhang, Y.P. Lei, M. Kodama, and T. Ishide: *J. Phys. D*, 2011, vol. 44 (48), p. 485302.
29. W.H. Zhang, J. Zhou, and H.L. Tsai: *Proc. SPIE*, 2003, vol. 4831, pp. 180–84.
30. E.H. Amara and R. Fabbro: *J. Phys. D*, 2008, vol. 41 (5), p. 055503.
31. L.J. Zhang, J.X. Zhang, G.F. Zhang, W. Bo, and S.L. Gong: *J. Phys. D*, 2011, vol. 44 (13), p. 135201.
32. S. Tsukamoto: *Sci. Technol. Weld. Join.*, 2011, vol. 16 (1), pp. 44–55.
33. S. Katayama, S. Kohsaka, M. Mizutani, K. Nishizawa, and A. Matsunawa: *Proceedings of ICALEO*, 1993, pp. 487–97.
34. S. Katayama, N. Seto, M. Mizutani, and A. Matsunawa: *Proceedings of ICALEO, Section C*, 2000, pp. 16–25.
35. S. Katayama, M. Mizutani, and A. Matsunawa: *Proc. SPIE*, 2003, vol. 4831, pp. 281–88.
36. A. Matsunawa, J. Kim, N. Seto, M. Mizutani, and S. Katayama: *J. Laser Appl.*, 1998, vol. 10 (6), pp. 247–54.
37. A. Matsunawa, N. Seto, J. Kim, M. Mizutani, and S. Katayama: *Proc. SPIE*, 2000, vol. 3888, pp. 34–45.
38. A. Matsunawa, N. Seto, J. Kim, M. Mizutani, and S. Katayama: *Trans. JWRI*, 2001, vol. 30, pp. 13–27.
39. A. Matsunawa and S. Katayama: *Weld. Res. Abroad*, 2003, vol. 49 (4), pp. 27–38.
40. N. Seto, S. Katayama, and A. Matsunawa: *Proceedings of ICALEO, Section E*, 1999, pp. 19–27.
41. N. Seto, S. Katayama, and A. Matsunawa: *Q. J. Jpn. Weld. Soc.*, 2000, vol. 18, pp. 243–55.
42. N. Seto, S. Katayama, M. Mizutani, and A. Matsunawa: *Proc. SPIE*, 2000, vol. 3888, pp. 61–68.
43. N. Seto, S. Katayama, and A. Matsunawa: *Q. J. Jpn. Weld. Soc.*, 2001, vol. 19, pp. 600–09.
44. S. Tsukamoto, I. Kawaguchi, G. Arakane, and H. Honda: *Int. Congress on Applications of Lasers & Electro-Optics (ICALEO)*, Jacksonville, FL, 2001, pp. 400–08.
45. I. Kawaguchi, S. Tsukamoto, H. Honda, and G. Arakane: *International Congress on Applications of Lasers & Electro-Optics (ICALEO)*, Laser Institute of America, Section A, Orlando, FL, 2003, vol. 1006, pp. 168–75.
46. J.E. Blackburn and C.M. Allen: “Modulated Twin Spot and High Beam Quality Laser Welding of Titanium Alloys”, TWI Industrial Member Report, No. 967, 2010.
47. A. Kaplan, M. Mizutani, S. Katayama, and A. Matsunawa: *J. Phys. D*, 2002, vol. 35 (11), pp. 1218–28.
48. J.E. Blackburn: Ph.D. Thesis, University of Manchester, 2011.
49. W.F. Hughes and J.A. Brighton: *Schaum's Outline of Fluid Dynamics*, McGraw-Hill, New York, 1999.